

An Edge-on Regular Disk Galaxy at $z = 5.289$

HAOJING YAN,¹ BANGZHENG SUN,¹ AND CHENXIAOJI LING²

¹*Department of Physics and Astronomy, University of Missouri, Columbia, MO 65211, USA*

²*National Astronomical Observatories, Chinese Academy of Science, Beijing, 100101, China*

Abstract

While rotation-supported gas disks are known to exist as early as at $z \approx 7$, it is still a general belief that stellar disks form late in the Universe. This picture is now being challenged by the observations from the James Webb Space Telescope (JWST), which have revealed a large number of disk-like galaxies that could be at $z > 3$, with some being candidates at $z > 7$. As an early formation of stellar disks will greatly impact our theory of galaxy formation and evolution, it is important to determine when such systems first emerged. To date, there is only one confirmed case at $z > 5$ (“Twister-z5”) reported in the literature. Here we present D-CEERS-z5289, a stellar disk at $z = 5.289 \pm 0.001$ discovered using the archival JWST NIRC*am* imaging and NIRS*pec* spectroscopic data. This galaxy has a highly regular edge-on disk morphology, extends to ~ 6.2 kpc along its major axis, and has an effective radius of ~ 1.3 – 1.4 kpc. By analyzing its 10-band spectral energy distribution using four different tools, we find that it has a high stellar mass of $10^{9.5-10.0} M_{\odot}$. Its age is in the range of 330–510 Myr, and it has a mild star formation rate of 10 – $30 M_{\odot} \text{ yr}^{-1}$. It is conceivable that this galaxy assembled its stellar mass by secular growth. Unfortunately, the current spectroscopic data do not allow the derivation of its rotation curve. Nevertheless, the width of its H α line from the partial slit coverage on one side of the disk reaches $\sim 345 \text{ km s}^{-1}$, which suggests that it could be a fast-rotating system.

1. INTRODUCTION

In the hierarchical structure formation paradigm, it is generally believed that disk galaxies should form late in the cosmic history because major mergers, which happened frequently in early times, would destroy disks. In addition, AGN and/or stellar feedback would also limit the formation of disks. Indeed, stellar disks are usually seen at $z \approx 2$ and below, which is in line with this picture. On the other hand, significant rotation in extended gas (i.e., gas disk) has been observed at $z \approx 4$ – 7 (e.g., Hodge et al. 2012; Smit et al. 2018; Rizzo et al. 2020, 2021; Neeleman et al. 2020; Fraternali et al. 2021; Lelli et al. 2021; Tsukui & Iguchi 2021; Roman-Oliveira et al. 2023), which challenge this view. Encouragingly, recent zoom-in numerical simulations suggest that disks could form early and be sustainable. For example, Kretschmer et al. (2022) identified an early disk ($z \approx 3.5$) in their high-resolution simulations. Tamfal et al. (2022) simulated a Milky Way-size galaxy and found that its stellar disk was in place as early as $z \approx 8$. Presumably, the formation of stellar disks should lag behind that of gas disks because, in contrast to gas, stars are collisionless and harder to “cool” to form a disk. Therefore, it is important to determine from the observational side when the first stellar disks emerged in the Universe.

Over the past two years, a large number of candidate stellar disks have been found by the James Webb Space Telescope (JWST) at $z > 3$ (e.g., Fudamoto et al. 2022; Ferreira et al. 2022, 2023; Nelson et al. 2023a; Jacobs et al. 2023; Robertson et al. 2023; Kuhn et al. 2024), which suggest an early formation of stellar disks. Spectroscopic confirmation

of redshifts, however, is still very limited. Using NIRC*am* images, Wu et al. (2023) identified a submillimeter galaxy (SMG) at $z = 3.06$ as a grand-design spiral, which is the first confirmed stellar disk at $z > 3$. Its redshift was previously obtained at the Atacama Large Millimeter/submillimeter Array (ALMA). Nelson et al. (2023b) reported the discovery of “Twister-z5”, a fast-rotating disk galaxy at $z = 5.38$ identified by the NIRC*am* imaging and grism spectroscopic data. Recently, Ling et al. (2024) presented “COSBO-7”, a lensed SMG that has an intrinsic disk morphology based on the NIRC*am* images; it has photometric redshift of $z_{\text{ph}} > 7$ and a single emission line detected by ALMA suggesting $z = 7.455$.

In this *Letter*, we present D-CEERS-z5289, a galaxy at $z = 5.289$ with a very regular edge-on disk morphology. It is among a large sample of disk galaxies that we visually classified using the archival NIRC*am* data, and its accurate redshift was based on NIRS*pec* spectroscopy. We describe its morphology and photometry in Section 2 and its spectroscopy in Section 3. The analysis of its stellar population is given in Section 4. We conclude with a brief discussion and summary in Section 5. All magnitudes are in the AB system. We adopt the following cosmological parameters throughout: $H_0 = 71 \text{ km s}^{-1} \text{ Mpc}^{-1}$, $\Omega_M = 0.27$ and $\Omega_{\Lambda} = 0.73$.

2. IMAGING DATA

The most critical imaging data are those taken by the Cosmic Evolution Early Release Science (CEERS, PID 1345; Finkelstein et al. 2023) using NIRC*am*. The location of our target is covered in seven passbands: F115W, F150W, and F200W in the short wavelength (SW) channel, and F277W,

F356W, F410M, and F444W in the long wavelength (LW) channel. We reduced these data on our own using the JWST science calibration pipeline (hereafter referred to as the “pipeline”) version 1.9.4 in the processing “context” of `jwst_1046.pmap`, and the details of the procedures were described in Yan et al. (2023). For this work, we created the mosaics at the pixel scale of $0''.06$. We also made use of the HST data from the Cosmic Assembly Near-Infrared Deep Extragalactic Legacy Survey (CANDELS; Grogin et al. 2011; Koekemoer et al. 2011), which are the ACS F606W and F814W and the WFC3 F125W images. Our source is located at R.A. = 14:19:38.33 and decl. = 52:55:23.10 (J2000.0). Table 1 summarizes the effective exposure times at this location in all these bands.

2.1. Morphology

Figure 1 shows the stamp images of our target in the aforementioned JWST and HST passbands as well as the color composite using these data. Its edge-on disk morphology is clearly revealed in the four NIRC*am* LW bands, and the disk extends to at least $\sim 1''.0$ along its major axis. To obtain quantitative assessments of its morphology, we utilized the GALFIT software (Peng et al. 2002, 2010) to model this galaxy in these four bands.

Running GALFIT needs the point spread function (PSF) of the image to be analyzed. We constructed the empirical point spread functions (PSFs) following the procedures of Ling & Yan (2022). For a given band, we selected isolated stars and made cutouts of 201×201 pixels centered on them. The sources around the stars were masked, and the cutout images were subsampled to a finer grid by 10 times. The centers of these cutouts were also aligned in this process. The fluxes of the stars were normalized to unity, and the normalized images were stacked using median. The stacked star image was rebinned by a factor of 10 in both dimensions to restore the original resolution. Finally, we cut out the central 101×101 pixels of the rebinned image, which was adopted as the PSF image. While GALFIT would only be run on the LW images, the PSFs were generated for all the bands as they would be used for photometry (see Section 2.2).

The GALFIT modeling was done on $6'' \times 6''$ cutouts, which contain some unrelated sources and contaminants. These could affect the modeling and must be removed. For each image, we estimated the mean value and rms of the background using `sigma_clip` in ASTROPY and then created a pseudo background map based on the mean and rms values. Any undesired pixels were then replaced by those from the pseudo background map. GALFIT was run on the final images that contain the target galaxy at the center with a clean background that preserves the original noise property.

This galaxy was successfully fitted by using a single Sérsic profile (Sérsic 1963) in the four NIRC*am* LW bands. As show in Figure 2, the results in these bands are consistent, with the Sérsic index n of 0.83–1.43, the effective radius R_e of $0''.21$ – $0''.22$, and the axis ratio b/a of 0.23–0.27. These results support that our object is an edge-on disk galaxy.

2.2. Photometry

Our NIRC*am* image products are registered to the astrometry of CANDELS, and all the images used in this work are aligned in pixel grid. These images were all PSF-matched to the angular resolution of the F444W image by convolving them with the convolution kernels created from the PSF images (see Section 2.1). We ran SEXTRACTOR (Bertin & Arnouts 1996) in the dual-image mode for photometry, using the F444W image for detection. We adopted the isophotal magnitudes (“MAG_ISO”) and estimated the errors using the rms maps that we derived using the ASTRORMS software tool¹. The results are reported in Table 1. For this isolated source of moderate brightness, the differences between MAG_ISO magnitudes and the total magnitudes (“MAG_AUTO”) are negligible. Our object is not detected in the HST ACS F606W band, for which we quote the 2σ limit calculated on the F606W rms map within the area of the same size as the isophotal aperture used in other bands.

We note that the NIRC*am* F115W data have to be discarded because the source is too close to the field edge in this band (see Figure 1), which leads to large error in photometry. Fortunately, the CANDELS HST WFC3 F125W image samples the similar wavelength range and compensates the loss.

Table 1. Summary of imaging data and photometry.

Filter	Exposure (s)	AB mag.
F606W	5066	≥ 28.72
F814W	11742	27.29 ± 0.26
F115W	1894	...
F125W	1813	26.49 ± 0.18
F150W	1119	26.63 ± 0.28
F200W	4751	26.17 ± 0.05
F277W	3083	25.63 ± 0.04
F356W	3082	25.52 ± 0.04
F410M	3082	25.12 ± 0.05
F444W	5650	25.33 ± 0.02

NOTE— The upper limit for F606W is the 2σ limit based on the rms map, calculated within a circle aperture equivalent to the isophotal area as defined in F444W and centered at the source location. The photometry in F115W is discarded because it is unreliable (due to the object being too close to the field edge in this band).

3. NIRSPEC SPECTROSCOPY

We used the public data from the RUBIES program (PID 4233; PIs de Graaff & Brammer), which is a spectroscopic survey in multiple fields (including CEERS) utilizing the

¹ Courtesy of M. Mechtley; see <https://github.com/mmechtley/astroRMS>

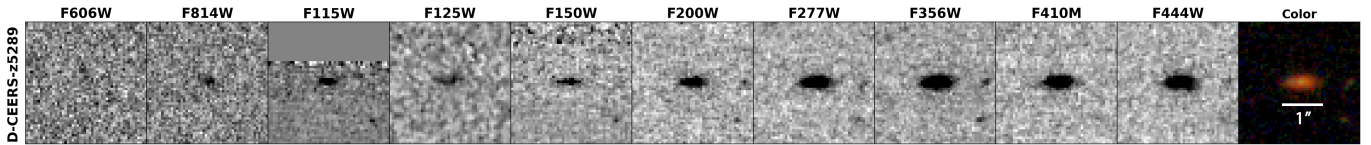


Figure 1. Image stamps of D-CEERS-z5289 ($3'' \times 3''$ in size). The bands are as labeled. The F606W, F814W and F125W images are from the HST CANDELS program, while all others are from the NIRCcam observations of the JWST CEERS program. The color image uses F606W + F814W + F115W + F125W + F150W as blue, F200W + F277W as green, and F356W + F410M + F444W as red. As the white line indicates, the galaxy extends at least $1''.0$ along its long axis.

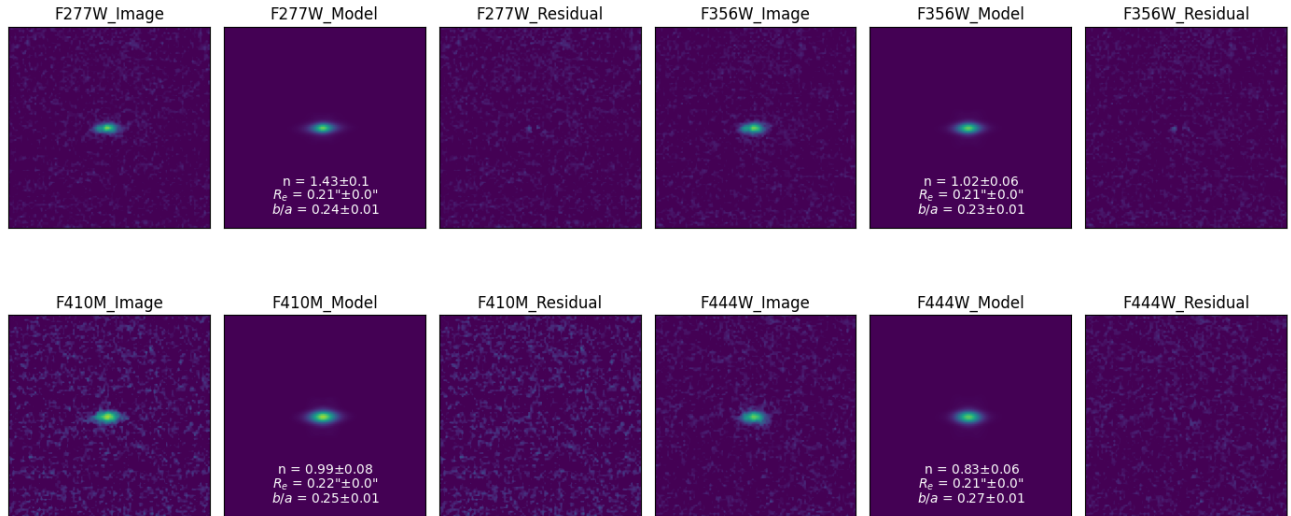


Figure 2. GALFIT fitting results in NIRCcam F277W, F356W, F410M, and F444W, using a single Sérsic profile. For each band, the original image, the best-fit model from GALFIT and the residual image after the model subtraction are shown from left to right. The values of the Sérsic index n , effective radius R_e , and axis ratio b/a are labeled on the model image.

NIRSpec multi-object spectroscopy mode with the micro-shutter assembly (MSA). The observations were done in a 3-slitlet configuration of open shutters with a 3-point nodding pattern, and the data were taken in both the PRISM/CLEAR (hereafter PRISM) and G395M/F290LP (hereafter G395M) disperser/filter setups with the same slit orientation. Under these setups, the spectral resolutions are $R \sim 100$ and ~ 1000 , and the wavelength coverages are $0.6\text{--}5.3 \mu\text{m}$ and $2.87\text{--}5.10 \mu\text{m}$, respectively. Overall, the total exposure time was ~ 2.84 ks in both setups.

To reduce these data, we first retrieved the Level 1b products from the Mikulski Archive for Space Telescopes (MAST) and processed them through the `calwebb_detector1` step of the pipeline (version 1.14.0) in the context of `jwst_1234.pmap`. The output “rate.fits” files were then processed through the MSAEXP package (Brammer 2023, version 0.8.4), which provides an end-to-end reduction including the final extraction of spectra. Briefly, the procedure removes the so-called “ $1/f$ ” noise pattern, detects and masks the “snowball” defects, subtracts the bias level, applies the flat-field, corrects the path-loss, does the flux calibration, traces spectra on all single exposures, and combines the single exposures with outlier rejection. The

background subtraction is done using the measurement in the nearest blank slit.

Our target is the source number 64132 in the RUBIES program, which was selected as a “filler” object. As shown in Figure 3, it was only partially covered by the slit. Nevertheless, the data are of sufficiently high quality to allow for the identification. The extracted 2D and 1D spectra are shown in Figure 3.

From the PRISM data, we identified five emission lines with $S/N \approx 3.5\text{--}18.5$: $[\text{O II}] \lambda 3727$, $\text{H}\beta$, $[\text{O III}] \lambda\lambda 4959, 5007$ doublet (unresolved), $\text{H}\alpha$, and $[\text{S II}] \lambda 6716$. Their observed wavelengths are 2.35 , 3.06 , 3.15 , 4.13 and $4.22 \mu\text{m}$, respectively, which put its redshift firmly at $z = 5.29 \pm 0.01$. Interestingly, the $\text{Ly}\alpha$ emission line is not visible, although the Lyman-break signature clearly presents. We fitted a 1D Gaussian profile to each of the five emission lines and measured the line intensities within $4 \times \text{FWHM}$ from the central wavelength, and the obtained values are listed in Table 2. A slight complication was that only one exposure was available over the range of $2.4\text{--}3.7 \mu\text{m}$: one exposure had no data in this range due to some unknown reasons, and one other had to be discarded because of the severe contamination. As a result, the spectrum in this section is contributed by only a single exposure (i.e., with

only 1/3 of the total integration time), and some contaminants cannot be removed. Upon close examination, we found that the $H\beta$ line was affected by such a contaminant very nearby. To remedy this, we performed the Gaussian fit of this line by setting the initial guess of its central wavelength based on the position of the $H\alpha$ line and that of its FWHM to $0.001 \mu\text{m}$. The $H\beta$ line was successfully separated from the contaminant in this way, although its intensity measurement inevitably had a large error.

In the G395M data, the spectrum does not cover $\lambda_{\text{obs}} \lesssim 3.32 \mu\text{m}$, presumably because the target was at the edge of the detector, causing the observed spectrum to truncate. We were still able to identify $H\alpha$ in this higher resolution setting; with the observed wavelength of $4.127 \pm 0.001 \mu\text{m}$ of this line, the redshift of the galaxy is refined to 5.289 ± 0.001 . The FWHM of the line is $47.5 \pm 2.9 \text{ \AA}$, which translates to $\Delta v_{H\alpha} = 345 \pm 21 \text{ km/s}$. This reflects the contributions from both the rotation and the random motion in the part of the galaxy covered by the slit, however these two components cannot be separated in the current data. The line intensity was measured in the same way as in the PRISM data, and the value is also reported in Table 2. The measurements from both settings agree within the errors. The weaker [S II] $\lambda 6716$ line was not detected in this setup, which is likely due to its lower sensitivity as compared to the PRISM setup.

Table 2. Line intensity measurements.

Emission Line	Intensity ($10^{-18} \text{ erg s}^{-1} \text{ cm}^{-2}$)
[O II] $\lambda 3727$	2.03 ± 0.35
$H\beta$	0.59 ± 0.16
[O III] $\lambda\lambda 4959, 5007$	3.78 ± 0.29
$H\alpha$	2.40 ± 0.13 $2.61 \pm 0.18^\dagger$
[S II] $\lambda 6716$	0.52 ± 0.15

NOTE—The value for $H\alpha$ marked with \dagger is obtained from the G395M observations, while all others are based on the PRISM observations.

As we have the measurements for both $H\alpha$ and $H\beta$ from the PRISM data, we can derive the extinction value through their line ratio, bearing in mind the caveat that the result is subject to the large error of the $H\beta$ line. The observed ratio between $H\alpha$ and $H\beta$ is $R_{\text{obs}} = 4.07 \pm 1.12$, while the intrinsic ratio in Case B recombination is $R_{\text{int}} = 2.86$. Using the extinction curve of Calzetti et al. (2000), the reddening is

$$E(B - V)_{\text{gas}} = \frac{\log_{10}(R_{\text{obs}}/R_{\text{int}})}{0.4(k_{H\beta} - k_{H\alpha})} = 0.30 \pm 0.20, \quad (1)$$

where $k_{H\alpha} = 3.327$ and $k_{H\beta} = 4.598$. The extinction at the location of the $H\alpha$ line is therefore $A(H\alpha) = k_{H\alpha} \times E(B - V) = 1.00 \pm 0.67$. After correction for the extinction, the intrinsic intensity of the $H\alpha$ line is $(6.03 \pm 3.68) \times$

$10^{-18} \text{ erg s}^{-1} \text{ cm}^{-2}$, which corresponds to the line luminosity of $L_{H\alpha} = (1.86 \pm 1.14) \times 10^{42} \text{ erg/s}$. If using the G395M measurement of the line and applying the same correction, its intrinsic intensity is $(6.53 \pm 4.01) \times 10^{-18} \text{ erg s}^{-1} \text{ cm}^{-2}$ and the line luminosity is $(2.03 \pm 1.24) \times 10^{42} \text{ erg/s}$. Note that the slit only covered part of the galaxy, and therefore these values are only lower limits; if the galaxy is uniform in its $H\alpha$ line emission, the total values should be at least twice as high.

Using the formalism of Kennicutt (1998) that converts the $H\alpha$ line luminosity to the instantaneous star formation rate (SFR), the values quoted above correspond to $\text{SFR}_{H\alpha}$ of 14.8 ± 9.0 and $16.1 \pm 9.8 M_{\odot}/\text{yr}$, respectively. Again, these are only lower limits due to the partial slit coverage.

4. SED ANALYSIS

To further study the stellar populations of D-CEERS-z5289, we fitted its spectral energy distribution (SED) constructed from the photometry reported in Table 1. In order to test the robustness of the results, we employed four different fitting tools: EAZY-py (Brammer et al. 2008, version 0.6.8), CIGALE (Burgarella et al. 2005; Noll et al. 2009; Boquien et al. 2019) version 2022.1 (Yang et al. 2022), BAGPIPES (Carnall et al. 2018, version 1.0.4), and PROSPECTOR (Leja et al. 2017; Johnson et al. 2021, version 1.3.0). The fitting was done at the fixed redshift of 5.29, and we used the Calzetti extinction law.

In the EAZY-py run, we used the “tweak_fsps_QSF_12_v3” templates, which are a modified version of the flexible stellar population synthesis models (FSPS; Conroy & Gunn 2010) tailored for galaxies at high redshifts (Finkelstein et al. 2022; Larson et al. 2023). These templates use the initial mass function (IMF) of Kroupa (2001).

For CIGALE, we used the stellar population synthesis models of Bruzual & Charlot (2003, “BC03”) with the IMF of Chabrier (2003). We adopted the delayed- τ star formation history (SFH), where $\text{SFR} \propto te^{-t/\tau}$ and τ could vary from 0 to 10 Gyr. The metallicity was freed within a set of numbers available in the program, with Z ranging from 0.0001 to 0.05. We also added contribution from nebula emission, and the ionization parameter was set to vary in $-4 \leq \log(U) \leq -2$. The dust reddening parameter $E(B - V)_{\text{star}}$ could vary from 0 to 1.5 mag.

BAGPIPES utilizes the BC03 models with the Kroupa IMF. We ran it using the exponentially decaying SFH (the “ τ model”), which is in the form of $\text{SFR} \propto e^{-t/\tau}$. We set τ as a free parameter varying between 10 Myr and 15 Gyr. The metallicity was allowed to vary in the range of $0 \leq Z/Z_{\odot} \leq 2.5$, and A_V could change from 0 to 8 mag. We also included the nebula emission lines and allowed the ionization parameter to vary in the range of $-4.0 \leq \log(U) \leq 2.0$.

In the PROSPECTOR run, we used the series of FSPS models of the delayed- τ SFH available in its template library. We adopted the same parameters as in the BAGPIPES run.

Table 3 summarizes the most critical physical parameters derived from the SED analysis, and Figure 4 shows the corresponding template spectrum in each run superposed on

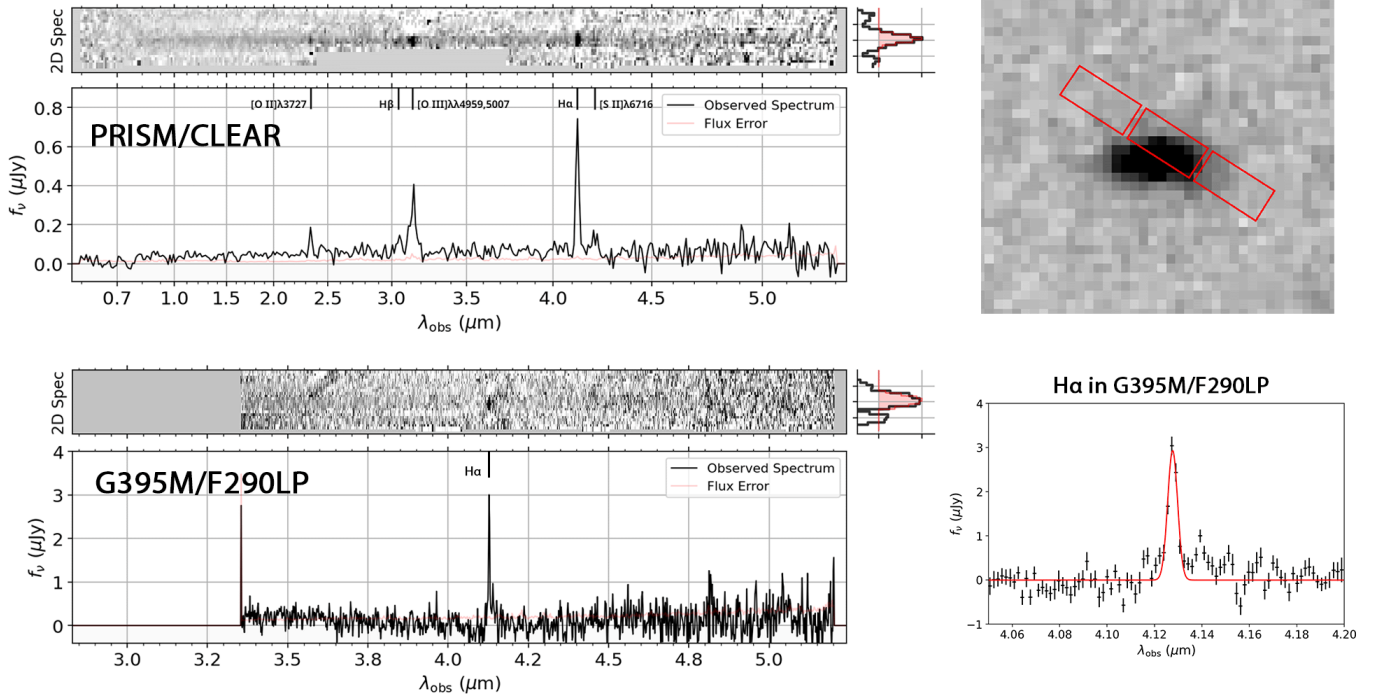


Figure 3. Results of the NIRSpec spectroscopy. The left two panels display the 2D and 1D spectra from the PRISM and G395M observations, respectively. In each 1D-spectrum plot, the spectrum is shown in black and the error is shown in light red. The identified lines are labeled. The histogram attached to the right side of each 2D spectrum shows the cross-dispersion direction plot of the inverse-weighted sum of the 2D spectrum in the dispersion direction, and the 1D spectrum is generated by weight-averaging pixels along the cross-dispersion direction with weights as described by the histogram. The upper-right panel shows the slit (red rectangles) overlaid on the F444W image ($2''3 \times 2''3$ in size); only part of the galaxy was covered by the slit. The lower-right panel is a zoom-in view to the region of the $H\alpha$ emission line in the G395M 1D spectrum, where the red line represents the best-fit Gaussian profile to the data (black plus symbols).

the observed SED. D-CEERS-z5289 appears to have stellar mass of $10^{9.5-10.0} M_{\odot}$, with an age of 330–510 Myr (i.e., formation redshift $z_f \approx 7.0-8.5$). The inferred SFR ranges from 8.2 to 18.0 $M_{\odot} \text{ yr}^{-1}$, which is broadly consistent with the lower limit of 14.8–16.1 $M_{\odot} \text{ yr}^{-1}$ derived from the measurements of the $H\alpha$ line obtained from only part of the galaxy (see Section 3). The derived dust extinction A_V for stars range from 0.3 to 1.0 mag, or equivalently, $E(B - V)_{\text{star}} = 0.07-0.25$ mag. Considering $E(B - V)_{\text{star}} = 0.44 \times E(B - V)_{\text{gas}}$, this is in reasonable agreement with the value of $E(B - V)_{\text{gas}} = 0.30 \pm 0.20$ mag obtained from the Balmer decrement (see Section 3). Not surprisingly, the metallicity parameter has a very wide range because it is very difficult (if not impossible) to derive metallicity based on broad-band photometry.

5. DISCUSSION AND SUMMARY

While the existence of high-redshift (up to $z = 6.8$) fast-rotating gas disks had been known for some years, it was unclear whether there are stellar disks at comparable redshifts. The JWST observations over the past two years indicate that there could be abundant stellar disks at $z > 3$, and the extreme case of COSBO-7 even suggests that stellar disks could emerge as early as $z > 7$. The vast majority of these studies,

however, rely on photometric redshifts, and the confirmed cases are still scarce.

This work shows that D-CEERS-z5289 is an edge-on disk galaxy at $z = 5.289$, extending ~ 6.2 kpc along its major axis with R_e of $\sim 1.3-1.4$ kpc. Its disk morphology is quantitatively verified in four NIRCcam bands that correspond to the rest frame wavelength range of 0.44–0.70 μm . To date, it is one of the only two *confirmed* disk galaxies at $z > 5$, with its redshift only slightly less than Twister-z5, a fast-rotating disk at $z = 5.38$. On the other hand, D-CEERS-z5289 has a very regular disk morphology, while Twister-z5 has a highly asymmetric disk with a dominant bulge. In this sense, D-CEERS-z5289 is a better representative of disk galaxies as we know them. To maintain its disk, D-CEERS-z5289 must be supported by rotation. While the current spectroscopic data do not allow the derivation of its rotation speed, the large width of the $H\alpha$ line ($\sim 345 \text{ km s}^{-1}$) over part of the galaxy on one side of its disk indicates that the rotation speed is likely significant.

D-CEERS-z5289 has stellar mass of $\sim 10^{9.5-10.0} M_{\odot}$, and it is conceivable that this is acquired through secular growth. Its current SFR, based on either the $H\alpha$ line measurement from part of the galaxy or the SED analysis on the galaxy as a whole, is at the level of $\sim 10-30 M_{\odot} \text{ yr}^{-1}$.

Table 3. Fitted physical properties from SED analysis.

Tool	EAZY-py	CIGALE	Bagpipes	Prospector
$\log_{10}(M/M_{\odot})$	$9.48^{+0.04}_{-0.03}$	9.53 ± 0.15	$9.65^{+0.13}_{-0.15}$	$10.01^{+0.17}_{-0.23}$
Age [Gyr]	...	0.51 ± 0.31	$0.33^{+0.33}_{-0.16}$	$0.35^{+0.36}_{-0.16}$
SFR	$8.15^{+3.25}_{-0.85}$	17.99 ± 10.09	$12.28^{+5.86}_{-4.25}$	14.26
A_V	$0.32^{+0.20}_{-0.07}$...	$0.59^{+0.18}_{-0.19}$	$1.04^{+0.16}_{-0.13}$
$E(B - V)_{\text{star}}$...	0.19 ± 0.05
Z/Z_{\odot}	...	1.77 ± 1.53	$1.45^{+0.75}_{-0.86}$	$0.03^{+0.09}_{-0.02}$

NOTE—For EAZY-py, the best-fit parameters are listed. For other three tools, the 50th percentile posterior values are reported. Star formation rates (SFRs) are in units of $M_{\odot} \text{ yr}^{-1}$. $E(B - V)_{\text{star}}$ is the reddening for stars, and $E(B - V)_{\text{star}} = 0.44 \times E(B - V)_{\text{gas}}$. For the Calzetti extinction law, $A_V = 4.05 \times E(B - V)_{\text{star}}$. We adopt $Z_{\odot} = 0.013$. Age and metallicity are not fitted parameters in our EAZY-py run using the adopted templates.

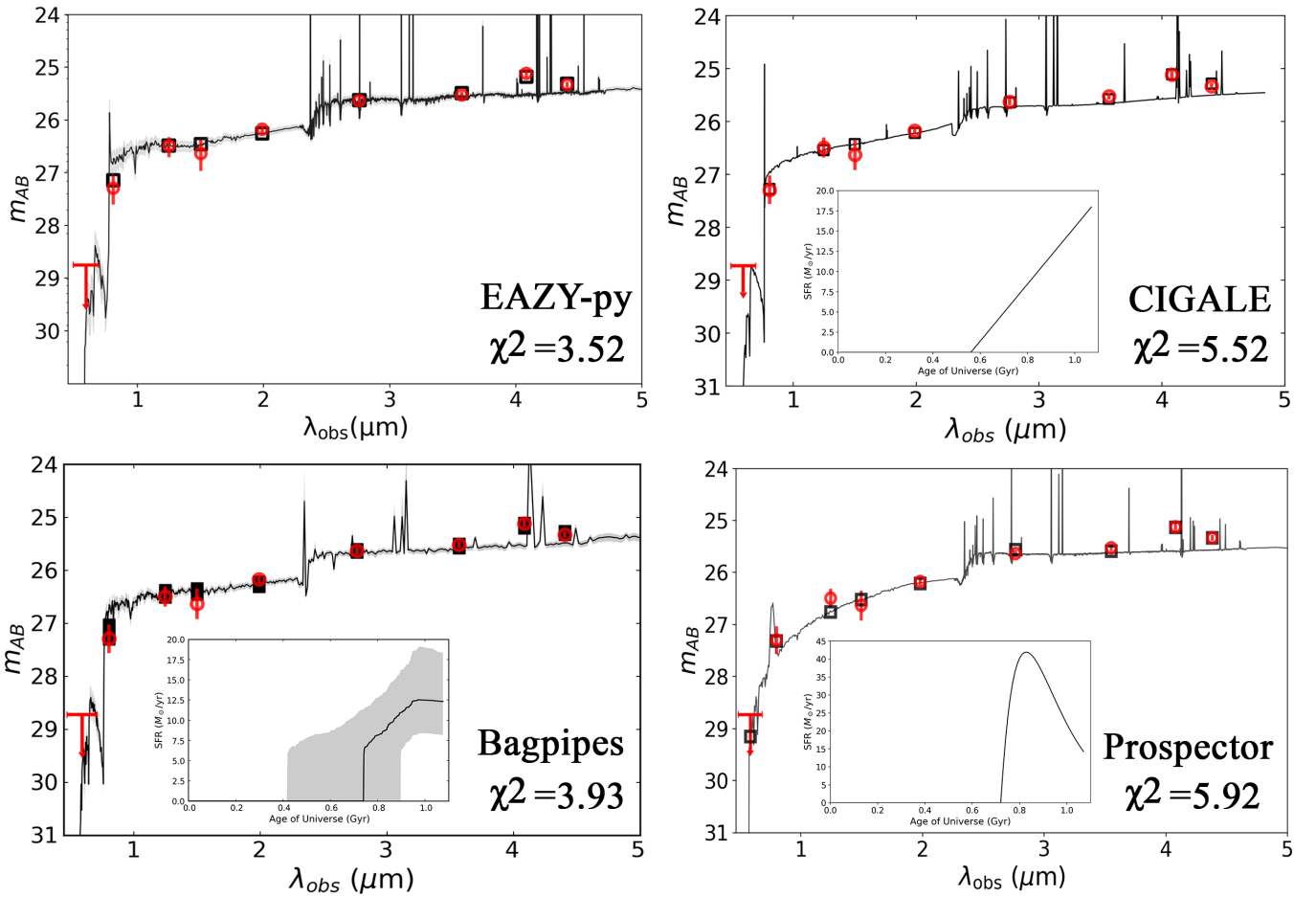


Figure 4. Fitted template spectrum (black curve) superposed on the SED (red symbols) in four fitting runs using different tools as labeled. The black squares are the synthesized magnitudes from these template spectra. The corresponding χ^2 values are also noted. For EAZY-py, the spectrum is that of the best-fit template. For CIGALE, BAGPIPES and PROSPECTOR, it is the 50th percentile posterior spectrum. The evolution of SFR (as a function of time; 50th percentile posterior value) is available for the latter three runs, which is shown in the inset in each of these three panels. The shaded area in that of the BAGPIPES run indicates the 16th to 84th percentile range.

Such a regular stellar disk in such an early time of the Universe (only ~ 1.1 Gyr after the Big Bang) will put strong constraints on the new picture of disk galaxy formation that is

now emerging. To connect to the dark matter halo that it resides, dynamic mass from its kinematics would be in demand. This calls for a proper measurement of its rotation

curve, which can be done by the JWST integral field spectroscopy.

1 All the JWST data used in this paper can be found in
2 MAST: [10.17909/bkqy-aj40](https://mast.stsci.org/#/search/10.17909/bkqy-aj40).

3 This work is based on the observations made with the
4 NASA/ESA/CSA James Webb Space Telescope and ob-
5 tained from the Mikulski Archive for Space Telescopes,
6 which is a collaboration between the Space Telescope Sci-
7 ence Institute (STScI/NASA), the Space Telescope European
8 Coordinating Facility (ST-ECF/ESA), and the Canadian As-
9 tronomy Data Centre (CADC/NRC/CSA).

10 H.Y. and B.S. acknowledge the support from the Univer-
11 sity of Missouri Research Council grant URC-21-005 and
12 the NSF grant AST-2307447. C.L. acknowledges the support
13 from the Special Research Assistant program of the Chinese
14 Academy of Sciences (CAS).

REFERENCES

- Bertin, E., & Arnouts, S. 1996, *A&AS*, 117, 393,
doi: [10.1051/aas:1996164](https://doi.org/10.1051/aas:1996164)
- Boquien, M., Burgarella, D., Roehlly, Y., et al. 2019, *A&A*, 622,
A103, doi: [10.1051/0004-6361/201834156](https://doi.org/10.1051/0004-6361/201834156)
- Brammer, G. 2023, *msaexp: NIRSspec analysis tools*, 0.6.17,
Zenodo, doi: [10.5281/zenodo.8319596](https://doi.org/10.5281/zenodo.8319596)
- Brammer, G. B., van Dokkum, P. G., & Coppi, P. 2008, *ApJ*, 686,
1503, doi: [10.1086/591786](https://doi.org/10.1086/591786)
- Bruzual, G., & Charlot, S. 2003, *MNRAS*, 344, 1000,
doi: [10.1046/j.1365-8711.2003.06897.x](https://doi.org/10.1046/j.1365-8711.2003.06897.x)
- Burgarella, D., Buat, V., & Iglesias-Páramo, J. 2005, *MNRAS*,
360, 1413, doi: [10.1111/j.1365-2966.2005.09131.x](https://doi.org/10.1111/j.1365-2966.2005.09131.x)
- Calzetti, D., Armus, L., Bohlin, R. C., et al. 2000, *ApJ*, 533, 682,
doi: [10.1086/308692](https://doi.org/10.1086/308692)
- Carnall, A. C., McLure, R. J., Dunlop, J. S., & Davé, R. 2018,
MNRAS, 480, 4379, doi: [10.1093/mnras/sty2169](https://doi.org/10.1093/mnras/sty2169)
- Chabrier, G. 2003, *PASP*, 115, 763, doi: [10.1086/376392](https://doi.org/10.1086/376392)
- Conroy, C., & Gunn, J. E. 2010, *ApJ*, 712, 833,
doi: [10.1088/0004-637X/712/2/833](https://doi.org/10.1088/0004-637X/712/2/833)
- Ferreira, L., Adams, N., Conselice, C. J., et al. 2022, *ApJL*, 938,
L2, doi: [10.3847/2041-8213/ac947c](https://doi.org/10.3847/2041-8213/ac947c)
- Ferreira, L., Conselice, C. J., Sazonova, E., et al. 2023, *ApJ*, 955,
94, doi: [10.3847/1538-4357/accc76](https://doi.org/10.3847/1538-4357/accc76)
- Finkelstein, S. L., Bagley, M., Song, M., et al. 2022, *ApJ*, 928, 52,
doi: [10.3847/1538-4357/ac3aed](https://doi.org/10.3847/1538-4357/ac3aed)
- Finkelstein, S. L., Bagley, M. B., Ferguson, H. C., et al. 2023,
ApJL, 946, L13, doi: [10.3847/2041-8213/acade4](https://doi.org/10.3847/2041-8213/acade4)
- Fraternali, F., Karim, A., Magnelli, B., et al. 2021, *A&A*, 647,
A194, doi: [10.1051/0004-6361/202039807](https://doi.org/10.1051/0004-6361/202039807)
- Fudamoto, Y., Inoue, A. K., & Sugahara, Y. 2022, *ApJL*, 938, L24,
doi: [10.3847/2041-8213/ac982b10.48550/arXiv.2208.00132](https://doi.org/10.3847/2041-8213/ac982b10.48550/arXiv.2208.00132)
- Grogin, N. A., Kocevski, D. D., Faber, S. M., et al. 2011, *ApJS*,
197, 35, doi: [10.1088/0067-0049/197/2/35](https://doi.org/10.1088/0067-0049/197/2/35)
- Hodge, J. A., Carilli, C. L., Walter, F., et al. 2012, *ApJ*, 760, 11,
doi: [10.1088/0004-637X/760/1/11](https://doi.org/10.1088/0004-637X/760/1/11)
- Jacobs, C., Glazebrook, K., Calabrò, A., et al. 2023, *ApJL*, 948,
L13, doi: [10.3847/2041-8213/accd6d](https://doi.org/10.3847/2041-8213/accd6d)
- Johnson, B. D., Leja, J., Conroy, C., & Speagle, J. S. 2021, *ApJS*,
254, 22, doi: [10.3847/1538-4365/abef67](https://doi.org/10.3847/1538-4365/abef67)
- Kennicutt, Robert C., J. 1998, *ApJ*, 498, 541, doi: [10.1086/305588](https://doi.org/10.1086/305588)
- Koekemoer, A. M., Faber, S. M., Ferguson, H. C., et al. 2011,
ApJS, 197, 36, doi: [10.1088/0067-0049/197/2/36](https://doi.org/10.1088/0067-0049/197/2/36)
- Kretschmer, M., Dekel, A., & Teyssier, R. 2022, *MNRAS*, 510,
3266, doi: [10.1093/mnras/stab3648](https://doi.org/10.1093/mnras/stab3648)
- Kroupa, P. 2001, *MNRAS*, 322, 231,
doi: [10.1046/j.1365-8711.2001.04022.x](https://doi.org/10.1046/j.1365-8711.2001.04022.x)
- Kuhn, V., Guo, Y., Martin, A., et al. 2024, *ApJL*, 968, L15,
doi: [10.3847/2041-8213/ad43eb](https://doi.org/10.3847/2041-8213/ad43eb)
- Larson, R. L., Hutchison, T. A., Bagley, M., et al. 2023, *ApJ*, 958,
141, doi: [10.3847/1538-4357/acfed4](https://doi.org/10.3847/1538-4357/acfed4)
- Leja, J., Johnson, B. D., Conroy, C., van Dokkum, P. G., & Byler,
N. 2017, *ApJ*, 837, 170, doi: [10.3847/1538-4357/aa5ffe](https://doi.org/10.3847/1538-4357/aa5ffe)
- Lelli, F., Di Teodoro, E. M., Fraternali, F., et al. 2021, *Science*,
371, 713, doi: [10.1126/science.abc1893](https://doi.org/10.1126/science.abc1893)
- Ling, C., Sun, B., Cheng, C., et al. 2024, *arXiv e-prints*,
[arXiv:2402.16649](https://arxiv.org/abs/2402.16649), doi: [10.48550/arXiv.2402.16649](https://doi.org/10.48550/arXiv.2402.16649)
- Ling, C., & Yan, H. 2022, *ApJ*, 929, 40,
doi: [10.3847/1538-4357/ac57c1](https://doi.org/10.3847/1538-4357/ac57c1)
- Neeleman, M., Prochaska, J. X., Kanekar, N., & Rafelski, M.
2020, *Nature*, 581, 269, doi: [10.1038/s41586-020-2276-y](https://doi.org/10.1038/s41586-020-2276-y)
- Nelson, E. J., Suess, K. A., Bezanson, R., et al. 2023a, *ApJL*, 948,
L18, doi: [10.3847/2041-8213/acc1e1](https://doi.org/10.3847/2041-8213/acc1e1)
- Nelson, E. J., Brammer, G., Gimenez-Arteaga, C., et al. 2023b,
arXiv e-prints, [arXiv:2310.06887](https://arxiv.org/abs/2310.06887),
doi: [10.48550/arXiv.2310.06887](https://doi.org/10.48550/arXiv.2310.06887)

- Noll, S., Burgarella, D., Giovannoli, E., et al. 2009, *A&A*, 507, 1793, doi: [10.1051/0004-6361/200912497](https://doi.org/10.1051/0004-6361/200912497)
- Peng, C. Y., Ho, L. C., Impey, C. D., & Rix, H.-W. 2002, *AJ*, 124, 266, doi: [10.1086/340952](https://doi.org/10.1086/340952)
- . 2010, *AJ*, 139, 2097, doi: [10.1088/0004-6256/139/6/2097](https://doi.org/10.1088/0004-6256/139/6/2097)
- Rizzo, F., Vegetti, S., Fraternali, F., Stacey, H. R., & Powell, D. 2021, *MNRAS*, 507, 3952, doi: [10.1093/mnras/stab2295](https://doi.org/10.1093/mnras/stab2295)
- Rizzo, F., Vegetti, S., Powell, D., et al. 2020, *Nature*, 584, 201, doi: [10.1038/s41586-020-2572-6](https://doi.org/10.1038/s41586-020-2572-6)
- Robertson, B. E., Tacchella, S., Johnson, B. D., et al. 2023, *ApJL*, 942, L42, doi: [10.3847/2041-8213/aca08610.48550/arXiv.2208.11456](https://doi.org/10.3847/2041-8213/aca08610.48550/arXiv.2208.11456)
- Roman-Oliveira, F., Fraternali, F., & Rizzo, F. 2023, *MNRAS*, 521, 1045, doi: [10.1093/mnras/stad530](https://doi.org/10.1093/mnras/stad530)
- Sérsic, J. L. 1963, *Boletín de la Asociación Argentina de Astronomía La Plata Argentina*, 6, 41
- Smit, R., Bouwens, R. J., Carniani, S., et al. 2018, *Nature*, 553, 178, doi: [10.1038/nature24631](https://doi.org/10.1038/nature24631)
- Tamfal, T., Mayer, L., Quinn, T. R., et al. 2022, *ApJ*, 928, 106, doi: [10.3847/1538-4357/ac558e](https://doi.org/10.3847/1538-4357/ac558e)
- Tsukui, T., & Iguchi, S. 2021, *Science*, 372, 1201, doi: [10.1126/science.abe9680](https://doi.org/10.1126/science.abe9680)
- Wu, Y., Cai, Z., Sun, F., et al. 2023, *ApJL*, 942, L1, doi: [10.3847/2041-8213/aca65210.48550/arXiv.2208.08473](https://doi.org/10.3847/2041-8213/aca65210.48550/arXiv.2208.08473)
- Yan, H., Sun, B., Ma, Z., & Ling, C. 2023, arXiv e-prints, arXiv:2311.15121, doi: [10.48550/arXiv.2311.15121](https://doi.org/10.48550/arXiv.2311.15121)
- Yang, G., Boquien, M., Brandt, W. N., et al. 2022, *ApJ*, 927, 192, doi: [10.3847/1538-4357/ac4971](https://doi.org/10.3847/1538-4357/ac4971)